

# 1 Coupled climate and subarctic Pacific nutrient upwelling over the last 850, 000 years

2  
3 Savannah Worne<sup>1\*</sup>, Sev Kender<sup>2,3\*</sup>, George E. A. Swann<sup>1</sup>, Melanie J. Leng<sup>3,4</sup>, and Ana  
4 Christina Ravelo<sup>5</sup>

5  
6 <sup>1</sup>Centre for Environmental Geochemistry, School of Geography, University of Nottingham,  
7 Nottingham, NG7 2RD, UK

8 <sup>2</sup>Camborne School of Mines, University of Exeter, Penryn Campus, Penryn, Cornwall, TR10  
9 9FE, UK

10 <sup>3</sup>British Geological Survey, Keyworth, Nottingham, NG12 5GG, UK

11 <sup>4</sup>Centre for Environmental Geochemistry, School of Biosciences, University of Nottingham,  
12 Sutton Bonington Campus, Loughborough, NE12 5RD, UK

13 <sup>5</sup>University of California, Santa Cruz, CA 95064, USA

14 \*Corresponding author. Email: [savannah.worne@nottingham.ac.uk](mailto:savannah.worne@nottingham.ac.uk); [s.kender@exeter.ac.uk](mailto:s.kender@exeter.ac.uk)

15  
16 **Highlights:** “Coupled climate and subarctic Pacific nutrient upwelling over the last 850, 000  
17 years”

- 18  
19
- Increased Bering Sea sea ice caused expansion of intermediate water in glacials
  - Intermediate water expansion inhibited deep water nutrient supply to surface waters
  - Region contributed to global ocean-air CO<sub>2</sub> exchange on glacial timescales
  - Tight correlation between subarctic nutrient upwelling and global CO<sub>2</sub>
- 22  
23

## 24 **Abstract**

25  
26 High latitude deep water upwelling has the potential to control global climate over glacial  
27 timescales through the biological pump and ocean-atmosphere CO<sub>2</sub> exchange. However, there  
28 is currently a lack of continuous long nutrient upwelling records with which to assess this

29 mechanism. Here we present geochemical proxy records for nutrient upwelling and glacial  
30 North Pacific Intermediate Water (GNPIW) formation in the Bering Sea over the past 850 kyr,  
31 which demonstrates that glacial periods were characterised by reduced nutrient upwelling,  
32 when global atmospheric CO<sub>2</sub> and temperature were also lowered. We suggest that glacial  
33 expansion of sea ice in the Bering Sea, and the simultaneous expansion of low nutrient GNPIW,  
34 inhibited vertical mixing and nutrient supply across the subarctic Pacific Ocean. Our findings  
35 lend support to the suggestion that high latitude sea ice and the resultant intermediate water  
36 formation, modulated deep water upwelling and ocean-atmosphere CO<sub>2</sub> exchange on glacial-  
37 interglacial timescales.

38 **Keywords:** Upwelling; Sea Ice; CO<sub>2</sub>; subarctic; Bering Sea; Glacial

39

## 40 **1. Introduction**

41

42 Recent studies have shown a sharp increase in both surface ocean subarctic Pacific productivity  
43 and CO<sub>2</sub> ventilation during the last deglaciation (Galbraith et al., 2007; Gray et al., 2018), and  
44 suggested that the equivalent of ~30 ppm atmospheric CO<sub>2</sub> was released into the atmosphere  
45 due to increased overturning (Rae et al., 2014). This was proposed to coincide with a collapse  
46 of glacial North Pacific Intermediate Water (GNPIW), allowing overturning to bring nutrient  
47 and CO<sub>2</sub>-rich deep water to the surface (Gray et al., 2018). Although a pervasive link between  
48 subarctic Pacific export productivity and Pleistocene glacial-interglacial cycles has been  
49 demonstrated (Jaccard et al., 2010, 2005), it is not yet known if this was primarily controlled  
50 by changes in iron supply (Galbraith et al., 2008; Praetorius et al., 2015), water column  
51 stratification and/or light limitation (Jaccard et al., 2010; Lam et al., 2013) and/or the extent of  
52 GNPIW (Knudson and Ravelo, 2015a; Li et al., 2017) and nutrient upwelling (Gray et al.,  
53 2018). If the upwelling of nutrient and CO<sub>2</sub>-rich water was the predominant control on subarctic

54 Pacific productivity variations (Kender et al., 2018), this would imply the region has been an  
55 active source of  $p\text{CO}_2$  throughout the Pleistocene and not just the last deglacial, because they  
56 are coupled with ice core temperature records (Jaccard et al., 2010, 2005). One way to test for  
57 GNPIW and its effect on upwelling nutrients is from the Bering Sea, which today contains an  
58 active upwelling zone.

59

60 Surface waters in the Bering Sea are fed by the subarctic Pacific Alaskan Stream, which enters  
61 through passes and straits in the Aleutian arc and circulates northward around the basin,  
62 forming the shelf-adjacent Bering Slope Current (BSC) (Stabeno et al., 1999) (Fig. 1).  
63 Turbulent eddies in the BSC extend below the surface waters at ~300 m water depth, causing  
64 upwelling of North Pacific Deep Water (NPDW), which contains some of the highest nutrient  
65 concentrations in the marine system (Stabeno et al., 1999). This seasonally raises photic zone  
66  $\text{CO}_2$  and fuels a high productivity region at the Bering shelf break, known as the “green belt”  
67 (Springer et al., 1996) (Fig. 1). Due to its terminal position in the ocean conveyor and deep  
68 bathymetric eddies, any glacial reduction in NPDW upwelling across the subarctic Pacific  
69 should also be apparent as reduced nutrient availability in the green belt.

70 Modern North Pacific Intermediate Water (NPIW) is sourced from the Okhotsk Sea and is  
71 widely distributed across the North Pacific ocean at a water depth between ~300 – 800 m  
72 characterized by salinity minima with density centred at  $26.8 \sigma_\theta$  (Talley, 1993; Yasuda, 1997).  
73 During the last glacial maximum, intensified NPIW (termed GNPIW) expanded down to 2000  
74 m (Matsumoto et al., 2002), with previous studies suggesting that the Bering Sea was a key  
75 source of GNPIW (Horikawa et al., 2010; Ohkushi et al., 2003) as a result of enhanced brine  
76 rejection on the Beringian shelf, following increased sea ice growth since ~900 kyr (Jang et al.,  
77 2017; Kender et al., 2018; Knudson and Ravelo, 2015b). Given its density, the formation of

78 GNPIW from the Bering Sea has the potential to suppress upwelling by preventing eddies in  
79 the BSC from reaching NPDW. Expansion of this low nutrient GNPIW from the Bering Sea  
80 would crucially act to enhance stratification across the subarctic region – not just the smaller  
81 Bering Sea – causing region-wide impact on vertical mixing, nutrient supply and the biological  
82 pump.

83

84 Here, we present a new high resolution long sedimentary nitrogen isotope record ( $\delta^{15}\text{N}$ ), in  
85 combination with previously published lower resolution results (Kim et al., 2017), from IODP  
86 Site U1343 in the Bering Sea green belt (Fig. 1) to assess variation in nitrate utilisation between  
87 Marine Isotope Stages (MIS) 1 and 21, where we assume that the sedimentary bulk  $\delta^{15}\text{N}$  is a  
88 representation of total macronutrient utilisation. To account for changes in export production,  
89 we normalise the opal mass accumulation rate (MAR) and produce the first high latitude record  
90 of nutrient delivery from deep to surface water (termed the “upwelling index”; see Methods).  
91 By semi-quantitatively assessing the offset between the opal MAR and  $\delta^{15}\text{N}$  in this way, we  
92 constrain the impact of local growth rate and iron supply, to reveal long-term variability in  
93 macronutrient supply from deep water upwelling. We also present a new high-resolution multi-  
94 species benthic foraminiferal oxygen isotope record for an improved age model and produce  
95 the first assessment of the influence of GNPIW at 2 km water depth in the Bering Sea. From  
96 this, we discuss the extent to which oceanographic changes in Bering Sea upwelling and  
97 GNPIW production may have contributed towards NPDW upwelling and glacial-interglacial  
98  $p\text{CO}_2$  changes in the subarctic Pacific over the last 850 kyr.

99

## 100 **2. Materials and Methods**

101       **2.1. Core materials**

102   IODP Site U1343 (54°33.4'N, 176°49.0'E, water depth 1950 m) is situated on a topographic  
103   high in the Bering Sea green belt adjacent to the northern continental shelf, proximal to the  
104   modern winter sea ice edge and at a depth just below the oxygen minimum zone (Fig. 1).  
105   Marine sediments are composed primarily of fine clays and biogenic material, and are  
106   characteristically distinct from shelf-transported materials (Takahashi et al., 2011).

107

108       **2.2. Foraminiferal isotopes**

109   Foraminiferal preservation is notably good at this site given the shallow North Pacific-wide  
110   lysocline which limits carbonate preservation at other Bering Sea sites (Takahashi et al., 2011),  
111   providing an excellent opportunity to create a robust high resolution  $\delta^{18}\text{O}_{\text{U1343}}$  age model  
112   (Asahi et al., 2016; Kender et al., 2018). In the absence of a single species consistently  
113   occurring in all samples, 262 samples of ~100  $\mu\text{g}$  of foraminiferal calcite were measured for  
114    $\delta^{18}\text{O}$  using ten different species of benthic foraminifera (*Cassidulina parkerianus*, *Cassidulina*  
115   *teretis*, *Elphidium batialis*, *Globobulimina auriculata*, *Globobulimina pacifica*, *Islandiella*  
116   *norcrossi*, *Nonionella labradorica*, *Uvigerina bifurcata*, *Uvigerina senticosa* and *Valvulineria*  
117   *spp.*) at an average sampling resolution of 0.84 m from 2 – 222 m CCSF-A. Measurements  
118   were made using an IsoPrime© mass spectrometer with a Multicarb device at the British  
119   Geological Survey, where the analytical precision of duplicates was <0.05‰. The stable  
120   isotope data were calibrated to the VPDB scale through the international NBS standards.  
121   Species-specific offsets from Kender et al. (2018) were applied to fit the data to the most  
122   commonly occurring species, *E. batialis*, and are presented in Figure 2 and Supplementary  
123   Table 2. Given that benthic foraminiferal  $\delta^{13}\text{C}$  is sensitive to diagenetic alteration, as calcite  
124   dissolution, re-precipitation and overgrowth can alter the isotopic composition of their tests

125 (Cook et al., 2016), poor linear regressions between foraminiferal  $\delta^{13}\text{C}$  and both raw  $\delta^{18}\text{O}$  ( $R^2$   
126 = 0.09,  $p < 0.001$ ) and  $\delta^{18}\text{O}$  adjusted to *E. batialis* ( $R^2 = 0.00$ ,  $p > 0.05$ ) confirms that diagenetic  
127 alteration of foraminiferal shells cannot explain the glacial-interglacial variability in the  $\delta^{18}\text{O}$   
128 (Fig. S1).

129

### 130 **2.3. Age Model, Sedimentation rates and Opal MAR calculations**

131 Benthic foraminiferal isotope data presented here were combined with previously published  
132 data from Site U1343 (Asahi et al., 2016), to create a total of 751  $\delta^{18}\text{O}_{\text{U1343}}$  data points with an  
133 average time step of 1.1 kyr at an average resolution of 0.30 m from 0 – 222 m CCSF-A. The  
134 age model, was defined by correlating to the LR04 global composite stack (Lisiecki and  
135 Raymo, 2005), and constructed by selecting 17 age-depth tie points during periods of rapid  
136 isotopic change primarily at deglacial intervals (Table S2). Although there is a possible time  
137 lag, where Pacific benthic  $\delta^{18}\text{O}$  records may lag the Atlantic Ocean (Asahi et al., 2016; Lisiecki  
138 and Raymo, 2005), the high sample resolution and strong correlation between  $\delta^{18}\text{O}_{\text{U1343}}$  and  
139 LR04 ( $r = 0.82$ ,  $p = < 0.001$ ) suggests that these are within the expected uncertainty of the age  
140 model.

141

142 The high sedimentation rate at IODP Site U1343 and a lack of hiatuses in core material provides  
143 confidence in the continuity of its record (Asahi et al., 2016; Takahashi et al., 2011). Based on  
144 the new composite age model, sedimentation rates were calculated between each age-depth tie  
145 point. The average sedimentation rate was  $29.15 \text{ cm kyr}^{-1}$ , with higher rates during interglacials  
146 and a notable sedimentation rate crash at ~630 kyr (likely due to low biogenic opal; Fig S2).  
147 These new sedimentation rates were applied to existing opal data (Kim et al., 2014) to calculate

148 an opal MAR record using linear interpolation of the ship dry bulk density data and a ten-point  
149 smoothing average (Takahashi et al., 2011).

150

## 151 **2.4. Bulk sedimentary $\delta^{15}\text{N}$**

152 Bulk samples at an average resolution of 0.81 m CCSF-A, totalling 276 samples between 0 –  
153 222 m CCSF-A were analysed for  $\delta^{15}\text{N}$  with 500 mg of raw material run on a Carlo Erba 1108  
154 elemental analyzer, interfaced to a Thermo Finnigan Delta Plus XP IRMS at the University of  
155 California, Santa Cruz, with a precision of 0.15‰ based on both sediment standards and  
156 replicates. Results, relative to atmospheric nitrogen (AIR), were combined with previously  
157 published data from Site U1343 (Kim et al., 2017), to produce a composite record of 373 data  
158 points ( $\delta^{15}\text{N}_{\text{U1343}}$ ), with an average resolution of 0.60 m between 0 and 222 m CCSF-A; average  
159 resolution of 2.3 kyr on the new age model (Fig. S2).

160

## 161 **2.5. Oceanographic indices**

### 162 **2.5.1. $\Delta\delta^{18}\text{O}_{849 - \text{U1343}}$**

163 To assess regional variation and discrepancies between Site U1343 and the deep North Pacific  
164 Ocean, a Pacific end-member record from ODP Site 849 (Mix et al., 1995) (0°11'N, 110°31'W;  
165 3851 m water depth) was used to remove high frequency and glacial-interglacial variability. A  
166 consistent offset of ~0.5 ‰ was found between  $\delta^{18}\text{O}_{\text{U1343}}$  and  $\delta^{18}\text{O}_{849}$ , and so this was added to  
167  $\delta^{18}\text{O}_{\text{U1343}}$  first, to ensure offset values reflected only differences in  $\delta^{18}\text{O}$  amplitude. After being  
168 linearly interpolated at an interval of 2 kyr (Fig. 2), a three-point smoothing spline was applied  
169 to the  $\delta^{18}\text{O}_{\text{U1343}}$ , and was subtracted from the similarly processed  $\delta^{18}\text{O}_{849}$  record ( $\Delta\delta^{18}\text{O}_{849 -$   
170  $\text{U1343}$ ), following a similar methodology to Knudson & Ravelo (2015a). Lower  $\delta^{18}\text{O}_{\text{U1343}}$

171 become more similar to those of shallower water Bering Sea Site U1342 at ~800 m water depth  
172 (Fig. 1, 3a), which is suggested to be influenced by GNPIW (Knudson and Ravelo, 2015a).  
173 Therefore, where  $\Delta\delta^{18}\text{O}_{849\text{-}U1343}$  is approximately 0, Site U1343 is assumed to reflect the same  
174 water mass as the deep North Pacific Ocean, which upwells along the Bering Sea shelf edge  
175 today (Stabeno et al., 1999). Whereas more positive  $\Delta\delta^{18}\text{O}_{849\text{-}U1343}$  values occur when  $\delta^{18}\text{O}_{U1343}$   
176 is lower than  $\delta^{18}\text{O}_{849}$ , suggesting a colder and/or more saline intermediate water mass is present  
177 at Site U1343, similar to the GNPIW signature at Site U1342.

178

### 179 **2.5.2. Upwelling Index**

180 To account for the changes in the isotope values of deep North Pacific source water ( $\delta^{15}\text{N}_{\text{source}}$ )  
181 and gain insights into regional nitrate utilisation, we follow previous work (Galbraith et al.,  
182 2008; Knudson and Ravelo, 2015b) by subtracting the record of ODP Site 1012 in the eastern  
183 tropical North Pacific (Liu et al., 2005) (32°17'N, 118°24'W; 1172 m water depth) which is  
184 influenced by waters from the Eastern Tropical North Pacific denitrification zone, and is  
185 thought to be a site of near complete nitrate utilisation throughout the Pleistocene (Galbraith et  
186 al., 2008).  $\delta^{15}\text{N}_{1012}$  was linearly interpolated at a time interval of 2 kyr (the average resolution  
187 of  $\delta^{15}\text{N}_{1012}$ ) and subtracted from the similarly interpolated  $\delta^{15}\text{N}_{U1343}$ , to produce a record driven  
188 by nutrient utilisation for Site U1343 ( $\Delta\delta^{15}\text{N}_{U1343\text{-}1012}$ ) (Fig S3).

189 Given that high  $\Delta\delta^{15}\text{N}_{U1343\text{-}1012}$  values can either reflect higher export production (more rapid  
190 removal of nitrate from the euphotic zone) or a slower nutrient resupply (slower replenishment  
191 of the surface nitrate pool), and as diatoms are the dominant contributors to export production,  
192 the opal MAR can be used to constrain the impact of variable productivity on  $\Delta\delta^{15}\text{N}_{U1343\text{-}1012}$ .  
193 Comparison of the opal MAR with the opal (%) confirms that the MAR record is not an artefact  
194 of the age model and calculated sedimentation rates (Fig S2). The opal MAR record was also



195 linearly interpolated at an interval of 2 kyr and then normalised so that all values ranged  
196 between 0 and 1. Then the similarly normalised  $\Delta\delta^{15}\text{N}_{\text{U1343-1012}}$  was subtracted to create a semi-  
197 quantitative proxy termed the ‘upwelling index’, with low (higher) values indicating decreased  
198 (increased) upwelling nutrient supply on the Bering shelf slope (Equation 1; Fig. 4b).

$$199 \quad \textit{Upwelling Index} = \textit{Normalised Opal MAR} - \textit{Normalised } \Delta\delta^{15}\text{N}_{\text{U1343-1012}} \quad (1)$$

200 In doing this we assume that the rate of export production is a reflection on total primary  
201 productivity, and that the majority of macronutrient delivery to the photic zone at IODP Site  
202 U1343 was from upwelling of NPDW and that rates of nutrient utilisation were controlled by  
203 both nutrient upwelling and delivery of iron (Fe) to the photic zone (predominantly derived  
204 from sea ice and shelf-derived material (Aguilar-Islas et al., 2008)). During times of low Fe  
205 input and incomplete nutrient utilisation, when increased upwelling will decrease nutrient  
206 utilisation (as the nutrient pool is larger) while productivity will show a smaller increase (from  
207 the small amount of upwelled Fe which will be scaled proportionally with macronutrient  
208 increase), causing the upwelling index to increase at a lower rate than for times of higher Fe  
209 delivery. The result of the upwelling index can be classified by three potential states which  
210 reflect interglacial, glacial and deglacial changes in biogeochemical cycling (Fig. 5).

211

## 212 **3. Results**

### 213 **3.1. $\Delta\delta^{18}\text{O}_{849 - \text{U1343}}$ : GNPIW formation**

214 Over the last 850 kyr benthic foraminiferal  $\delta^{18}\text{O}_{\text{U1343}}$  varied between +2.47 and +5.02 ‰ (mean  
215 = +3.58 ‰), with an amplitude of change similar to LR04 and ODP Site 849 in the eastern  
216 equatorial Pacific (range from +3.08 to +5.10 ‰; mean = +4.12 ‰; Fig. 3a, 4a). The highest  
217  $\Delta\delta^{18}\text{O}_{849-\text{U1343}}$  values occur during glacial maxima of MIS 4, 6, 8, 12, 16 and 20 (Fig. 3b). As

218 the two  $\delta^{18}\text{O}$  records are used to create the age models, with rapid deglacial changes in  $\delta^{18}\text{O}$  as  
219 the tie points, rapid  $\Delta\delta^{18}\text{O}_{849\text{-}U1343}$  shifts at deglacials may be artificially amplified. However,  
220  $\Delta\delta^{18}\text{O}_{849\text{-}U1343}$  values are significantly higher in glacial periods (mean = 0.05) than interglacial  
221 periods (mean = 0.00;  $p < 0.05$ ), with values gradually increasing as glacial periods developed  
222 and became more intense, suggesting an increasing influence of GNPIW in the Bering Sea  
223 slope region. During deglacial periods GNPIW collapses, and the  $\Delta\delta^{18}\text{O}_{849\text{-}U1343}$  becomes more  
224 negative during interglacials, as  $\delta^{18}\text{O}_{U1343}$  is more similar to the deep water record from the  
225 eastern equatorial Pacific Site 849, suggesting NPDW influence at the 2 km water depth at  
226 Bering Sea slope Site U1343.

227

### 228 **3.2. $\delta^{15}\text{N}$ and Opal MAR**

229 Today Bering Sea green belt primary productivity is dominated by diatoms which primarily  
230 bloom in spring/summer following seasonal sea ice melt, which provides a source of dissolved  
231 iron and promotes water column stability, allowing diatoms to remain in the photic zone and  
232 utilise available nutrients (Aguilar-Islas et al., 2008). Estimates of annual primary productivity  
233 in the green belt are  $>170 \text{ g C m}^{-2} \text{ yr}^{-1}$  (Sambrotto et al., 2008) with blooms sustained by tidal  
234 mixing and lateral supply of iron rich waters from the shelf (Aguilar-Islas et al., 2008).  
235 Conditions, however, are reversed during winter months (November to April) when sea ice  
236 expansion and associated reductions in light availability reduces primary productivity, leading  
237 to incomplete nutrient utilisation and the emergence of high-nutrient low chlorophyll (HNLC)  
238 conditions similar to the lower subarctic Pacific and central Bering Sea (Galbraith et al., 2008;  
239 Knudson and Ravelo, 2015b; Sambrotto et al., 2008). With diatoms as the primary contributors  
240 to biogenic material within the IODP Site U1343 sediment record (Takahashi et al., 2011), the  
241 opal mass accumulation (MAR) record, recalculated using sedimentation rates from our new

242 age model, is thought to approximate changes in primary productivity (Kim et al., 2014), where  
243 productivity was significantly higher in interglacials (mean = 3.30 g cm<sup>-2</sup> kyr<sup>-1</sup>) than in glacials  
244 (mean = 2.66 g cm<sup>-2</sup> kyr<sup>-1</sup>; p < 0.001; Fig. 3e) (Kim et al., 2014). Although the phytoplankton  
245 community structure will likely have varied in response to changing seasonality, diatoms have  
246 remained the dominant contributors to export production in the Bering Sea (Takahashi et al.,  
247 2011). As changes in the composition of the phytoplankton community will be minor in  
248 comparison to glacial-interglacial variation in export production, we assume these changes are  
249 unlikely to have impacted our geochemical signals on millennial timescales. Furthermore,  
250 silica supply is not considered a limiting nutrient in the Bering Sea (Tsunogai et al., 1979), and  
251 hence the opal MAR likely reflects first order changes in productivity (Kim et al., 2014).

252

253 Changes in  $\delta^{15}\text{N}_{\text{U1343}}$  are assumed to primarily reflect temporal variations in nitrate utilisation  
254 which is influenced by the amount of productivity and nutrient availability, which is in turn  
255 dependent on the rate of upwelling of macronutrient rich NPDW, driven by eddies in the BSC  
256 along the shelf break. Terrestrial input with low  $\delta^{15}\text{N}$  is not considered to have driven the record  
257 due to the lack of covariation of  $\delta^{15}\text{N}$  and sedimentary C/N ratio (Fig. S2), and the broad  
258 similarity with ODP Site 882 and MD2416 in the North Pacific which are far from land (Fig.  
259 3c) (Galbraith et al., 2008; Jaccard et al., 2010). Similarly, variable inorganic contribution is  
260 not considered to bias the bulk  $\delta^{15}\text{N}$  record, as the intercepts on %TOC vs. %TN do not vary  
261 significantly between glacial and interglacials (Fig. S4). In addition, diatom-bound  $\delta^{15}\text{N}$   
262 records from the Bering Sea and subarctic Pacific show similar trends to their bulk  $\delta^{15}\text{N}$   
263 counterparts (Brunelle et al., 2007; Galbraith et al., 2008; Studer et al., 2012), indicating bulk  
264 sediment nitrogen is a good proxy for nutrient utilisation in surface water.  $\delta^{15}\text{N}_{\text{U1343}}$  values

265 range from +2.72 to +8.89 ‰ (mean = +5.59 ‰) with peak values occurring in glacial,  
266 particularly during MIS 2 at ~14 kyr and MIS 8 at ~245 kyr (Fig. 2c).

267

268 Prior to ~ MIS 13, there appears to be less distinctive glacial-interglacial variability in  $\delta^{15}\text{N}$ -  
269  $\text{U}_{1343}$ , which could reflect sedimentary preservation, however diagenetic alteration of nitrogen  
270 is considered less of an influence in this high sedimentation rate setting (Brunelle et al., 2007;  
271 Robinson et al., 2012). Alternatively, the greater glacial-interglacial variability in nutrient  
272 utilisation over the last ~600 kyr may be expected, given that 100 kyr cycles in the late  
273 Quaternary are characterised by colder and more severe glacial periods, and warmer  
274 interglacial periods, than the preceding 41 kyr cycles (McClymont et al., 2013).

275

276 Low  $\delta^{15}\text{N}_{\text{U}_{1343}}$  excursions (< 4.5‰) may be a result of inorganic or terrestrial input, as the  
277 modern deep ocean average  $\delta^{15}\text{N}$  is ~4.5‰ (Sigman et al., 2009). However, the  $\delta^{15}\text{N}$  record is  
278 not a direct recorder of deep ocean  $\delta^{15}\text{N}$  and more likely reflects surface water  $\delta^{15}\text{N}$ , which will  
279 be a combination of the deep water signal, as well as surface water processes such as  
280 productivity. Confidence in the fidelity of low  $\delta^{15}\text{N}_{\text{U}_{1343}}$  values (<5.0‰) is provided by other  
281 subarctic Pacific records from open ocean sites great distances from the continent, such as from  
282 Site MD2416 (Galbraith et al., 2008), Site 882 (Jaccard et al., 2010) (Fig. 3c) and Site 887  
283 (Studer et al., 2012). Furthermore, diatom-bound  $\delta^{15}\text{N}$  results also show values less than 5‰  
284 in the subarctic (Brunelle et al., 2007; Studer et al., 2012). Although nitrate uptake can only  
285 account for increases in  $\delta^{15}\text{N}_{\text{U}_{1343}}$ , terrestrial/inorganic nitrogen input is unlikely to impose a  
286 first-order control on the glacial-interglacial variability at U1343.

287

### 288 3.3. Glacial-interglacial variability in the upwelling index

289 The upwelling index is highly correlated with the LR04 deep ocean  $\delta^{18}\text{O}$  record ( $r = -0.72$ ,  $p <$   
290  $0.001$ ) – a combination of global ice volume and deep ocean temperature – with a significantly  
291 lower upwelling index in glacials (mean =  $-0.40$ ) than in interglacials (mean =  $-0.10$ ;  $p < 0.001$ )  
292 (Fig. 4). Minimal upwelling index values during glacial maxima (due to increased rates of  
293 nitrate utilisation ( $\delta^{15}\text{N}_{\text{U1343}}$ ) despite lowered primary productivity (opal MAR)), suggest there  
294 was a smaller pool of nutrients in the photic zone, concomitant with expanded GNPIW (Fig.  
295 3b-c, e). We propose that presence of GNPIW was a pivotal mechanism in reducing nutrient  
296 supply from deep water upwelling (see Discussion). A rapid deglaciation phase occurred at all  
297 major glacial terminations (dashed lines in Fig. 4) when nutrient upwelling peaked, indicating  
298 ample nutrient supply from resumed NPDW upwelling and the establishment of a high  
299 productivity/low nitrate utilisation state.

300 Although upwelling is also correlated with relative sea level (Elderfield et al., 2012) ( $r = -0.55$ ,  
301  $p < 0.001$ ) and Antarctic air temperature (Jouzel et al., 2007) ( $r = 0.56$ ,  $p < 0.001$ ) (Fig. 4), the  
302 high correlation with global surface ocean temperature (Snyder, 2016) ( $r = 0.60$ ,  $p < 0.001$ ) and  
303 ice core atmospheric  $\text{CO}_2$  records over the last 800 kyr are of particular interest ( $r = 0.60$ ,  $p <$   
304  $0.001$ ) (Lüthi et al., 2008). These tight correlations are despite the limitations to our  
305 productivity and nutrient utilisation proxies and possible inter-site age model discrepancies,  
306 therefore suggesting a common link between upwelling, atmospheric temperature and  $\text{CO}_2$ .  
307 Although correlation does not imply causation, the consistency in the relationship between the  
308 upwelling index and the ice-core derived  $\text{CO}_2$  provides support for a shared underlying  
309 mechanism. Exceptions to this correlation between the upwelling index and  $\text{CO}_2$  occurs during  
310 MIS 13, when the upwelling index was high but  $p\text{CO}_2$  was lower than subsequent interglacials,  
311 and MIS 11, when the upwelling index was lower than might be expected given the higher

312  $p\text{CO}_2$  for this interglacial (Fig. 4). While the former discrepancy may be a result of the MAR  
313 calculations, where sedimentation is relatively high during MIS 13, this also correspond with  
314 the Mid-Brunhes Event (MBE) where interglacial conditions became warmer (Jouzel et al.,  
315 2007). A productivity peak at MIS 13 in response to increased sea ice melt may explain the  
316 high upwelling index result at this time. Alternatively, notably warm conditions during “super  
317 interglacial” MIS 11 (Melles et al., 2012) likely caused earlier and rapid sea ice melt, which  
318 would have reduced iron availability to the green belt, reducing the duration of the spring bloom  
319 and limiting summer productivity (Aguilar-Islas et al., 2008). After post-MBE warming, from  
320 MIS 11 onward, the relationship between upwelling index and Antarctic  $\text{CO}_2$  is particularly  
321 strong ( $r = 0.70$ ,  $p < 0.001$ ).

322

#### 323 **4. Discussion**

324 Changes in nutrient upwelling are likely to have been controlled by a combination of sea level  
325 change, sea ice presence and GNPIW extent (Kender et al., 2018). Geochemical and biological  
326 proxy evidence indicate that an expansion of sea ice occurred during glacials throughout the  
327 last 850 kyr (Detlef et al., 2018; Stroynowski et al., 2017; Teraishi et al., 2016), causing lower  
328 rates of primary productivity (Kim et al., 2014) and actively restricting air-sea gas exchange.  
329 Coincident with glacials and maximal sea ice extent, our  $\Delta\delta^{18}\text{O}_{849\text{-}U1343}$  results provide  
330 evidence for intermediate water presence to at least 2 km water depth, supporting data from  
331 IODP Site U1342 which indicates GNPIW presence to at least 800 m water depth (Knudson  
332 and Ravelo, 2015a) (Fig. 3a-b). Brine rejection on the Bering Sea shelf during enhanced sea  
333 ice formation in glacials is the proposed mechanism for formation of a more saline water body,  
334 which would sink to intermediate depths at the shelf slope and propagate southward as GNPIW  
335 (Knudson and Ravelo, 2015a), as observed for NPIW in the modern Okhotsk Sea.

336

337 Although direct sea ice reconstructions from the Bering Sea are of lower resolution, they  
338 broadly support GNPIW expansion, as glacial periods during this time interval were  
339 characterised by extended thick pack ice which peaked during the mid-to-late glacials, when  
340 we see the largest offsets in  $\Delta\delta^{18}\text{O}_{849\text{-U1343}}$  (Detlef et al., 2018; Stroynowski et al., 2017).  
341 Changes in sea-ice would have been in combination with sea level falls of ~50-150 m during  
342 glacials (Elderfield et al., 2012) (Fig. 4d), causing closure of the Bering Strait (modern depth  
343 of ~50 m) and retention of both cold/fresh surface waters and denser modified shelf-water  
344 (following brine rejection) within the Bering Sea, as the northward flow into the Arctic Ocean  
345 was prevented (Kender et al., 2018; Knudson and Ravelo, 2015a). The resultant expanded  
346 GNPIW at the shelf edge likely prevented eddies in the BSC from reaching NPDW, isolating  
347 nutrients in the photic zone without significant resupply (low upwelling index) and causing the  
348 observed high rates of nitrate utilisation but low productivity, whilst also trapping  $\text{CO}_2$  in deep  
349 waters during glacials over the last 850 kyr (Fig. 5b).

350

351 In addition to sea ice and GNPIW expansion during glacials triggering a reduction in  
352 productivity and nutrient upwelling, lowered sea level would have hindered Alaskan Stream  
353 water from flowing into the basin by shoaling the passes along the eastern Aleutian arc (Fig.  
354 1b). Although we cannot quantify this effect, it would have caused some degree of decrease in  
355 surface water flow around the Bering Sea basin. This is important because the strength of BSC  
356 flow controls eddy field fluctuation, where increased flow maintains higher primary  
357 productivity by promoting vertical nutrient supply, and vice versa (Mizobata and Saitoh, 2004).  
358 There is evidence for glacial reductions in the inflow of the Alaskan Stream from reduced  
359 proportions of the diatom species *Neodenticula seminae* near the inflow sites at the Aleutian

360 arc in the southern Bering Sea, as well as at the slope (Stroynowski et al., 2017; Teraishi et al.,  
361 2016). The resultant decrease in BSC flow in glacials would have therefore reduced large eddy  
362 formation, further lowering NPDW upwelling of nutrients, productivity and photic zone CO<sub>2</sub>  
363 (Mizobata and Saitoh, 2004). Simultaneously, sea ice expansion over a shallowed Beringian  
364 shelf during glacials may have increased the mobilisation of sediments and transport of shelf-  
365 derived iron to the slope (Aguilar-Islas et al., 2008). Reduced vertical macronutrient supply but  
366 sustained iron supply from sea ice, which is a key source of bioavailable iron in the green belt  
367 today (Aguilar-Islas et al., 2008), could help to explain the co-occurrence of low productivity  
368 and high nutrient utilisation in glacials (Fig. 2, 5b). Overall, our results support previous  
369 proposals that enhanced sea ice and GNPIW formation during periods of low glacial sea level  
370 were a key mechanism for controlling deep water upwelling and green belt nutrient supply over  
371 the last 850 kyr (Kender et al., 2018). Reduced upwelling of nutrient-rich NPDW due to  
372 GNPIW presence and lowered BSC strength and physical overturning in glacials could then  
373 have caused the green belt region to act as a larger net carbon sink.

374

375 During deglaciation, conditions would have reversed with the break up and retreat of sea ice  
376 (Kim et al., 2014; Stroynowski et al., 2017) and sea level rise, causing re-strengthening of the  
377 BSC and both local and regional collapse of GNPIW (Fig. 5b). Coupled with high shelf-derived  
378 iron from deglacial flooding of the Beringian shelf and potentially increased deglacial Yukon  
379 River flow (VanLaningham et al., 2009), this rapid restoration of regional upwelling nutrients  
380 explains the observed productivity peaks during deglaciations (Kim et al., 2014) from at least  
381 MIS 20-21 onwards. Modelling has shown that late in the last deglacial, wind strength across  
382 the Bering Sea and subarctic remained greatly increased due to the remanence of large North  
383 America ice sheets (Gray et al., 2018). This would have aided eddy formation in the Bering



384 Sea and upwelling of NPDW across the subarctic region through promoting vertical mixing.  
385 Once ice sheets had declined and sea ice diminished, seasonally variable upwelling and vertical  
386 mixing across the subarctic Pacific would have become re-established in interglacials, similar  
387 to modern conditions (Fig. 5c).

388

389 We have demonstrated for the first time that the glacial reductions in Bering Sea slope primary  
390 productivity were driven at least in part by reduced upwelling of nutrients (Fig. 4b), and  
391 propose that this was largely controlled by sea ice and expanded low- nutrient GNPIW (Fig.  
392 3b). Whilst we do not suggest that this mechanism solely explains the observed proxy evidence  
393 from across the North West Pacific Ocean during the Pleistocene, similar productivity and  
394 nutrient utilisation  $\delta^{15}\text{N}$  records are seen at ODP Site 882 and MD2416 (Fig. 3c, d, f) (Galbraith  
395 et al., 2008; Jaccard et al., 2010), whilst an upwelling index derived for ODP Site 882, using a  
396  $\Delta\delta^{15}\text{N}_{882-1012}$  record for regional nutrient utilisation and opal (%) as a productivity record  
397 (Jaccard et al., 2010) (Fig. 3d, f), shows remarkably similar trends to the Bering Sea upwelling  
398 index. Although the upwelling index for Site 882 only covers a short time period, the high  
399 correlation between the upwelling index for Sites U1343 and 882 ( $r = 0.77$ ,  $p < 0.001$ ) provides  
400 support for a common controlling mechanism of GNPIW between the Bering Sea and wider  
401 subarctic Pacific region.

402

403 We propose that reduced upwelling of nutrients in the subarctic Pacific Ocean, as recorded at  
404 ODP Site 882 and MD2416, was the cause of reduced glacial export production, forced by the  
405 expansion of low nutrient GNPIW, similar to the Bering Sea slope (at U1343). The formation  
406 of dense GNPIW in the Bering Sea likely propagated south through the deep western  
407 Kamchatka Strait (Fig. 1), although this does not discount additional contributions of NPIW

408 from the Okhotsk Sea (Max et al., 2014). This mechanism was proposed for the last glacial  
409 cycle in the subarctic Pacific Ocean, where model and proxy evidence from the Bering and  
410 Okhotsk Seas indicated that enhanced GNPIW during Heinrich Stadial 1 increased  
411 intermediate-to-deep ocean stratification, isolating abyssal carbon in NPDW (Gong et al.,  
412 2019). Furthermore, the disappearance of GNPIW during the latter part of last deglaciation  
413 allowed renewed upwelling of deeper water rich in nutrients and is considered responsible for  
414 increases in surface water proxies for CO<sub>2</sub> (Gray et al., 2018). Our new data support GNPIW  
415 production as the underlying mechanism driving the strength of nutrient upwelling both along  
416 the Bering Sea slope and across the open subarctic Pacific Ocean over the past 850 kyr.

417

418 Changes in the Southern Ocean are considered to be a dominant component in driving glacial-  
419 interglacial changes in *p*CO<sub>2</sub> (Gottschalk et al., 2016; Jaccard et al., 2013). For example, glacial  
420 reduction of atmospheric *p*CO<sub>2</sub> has been linked to an increased rate of biological sequestration  
421 in the Southern Ocean and/or reduced supply of nutrients and CO<sub>2</sub> upwelled from the deep  
422 ocean as a result of intermediate water formation and expanded sea ice cover (Sigman et al.,  
423 2010). Although net CO<sub>2</sub> flux in the Southern Ocean is regarded as the largest single control  
424 on glacial-interglacial variability in *p*CO<sub>2</sub> (Sigman et al., 2010), we demonstrate here that  
425 similar processes occurred in the subarctic Pacific region. With modelling studies suggesting  
426 that ~30 ppm atmospheric CO<sub>2</sub> was released into the atmosphere due to increased overturning  
427 in the subarctic region at the last deglaciation (Rae et al., 2014), we surmise that similar  
428 magnitude ocean-atmospheric CO<sub>2</sub> fluxes may have occurred over the last 850 kyr in response  
429 to changes in deep water nutrient upwelling across the Bering Sea and subarctic Pacific Ocean.  
430 This aids ongoing efforts to fully explaining observed trends in atmospheric *p*CO<sub>2</sub> over this  
431 interval (Gray et al., 2018; Rae et al., 2014).

## 432 **5. Conclusion**

433 Overall, we constructed a new high resolution benthic oxygen isotope stratigraphy for IODP  
434 Site U1343, to aid the development of a new nutrient upwelling index which uses  $\delta^{15}\text{N}_{\text{bulk}}$  and  
435 opal MAR to assess glacial-interglacial variability in the supply of nutrients from NPDW  
436 upwelled at the Bering shelf edge. We find a tight correlation between the upwelling index  
437 results and global temperature, sea level and atmospheric  $p\text{CO}_2$ , as well as the upwelling index  
438 calculated for the short term record at ODP Site 882 in the western subarctic Pacific Ocean.  
439 We posit that increased sea ice volumes in the Bering Sea and the resultant expansion of  
440 GNPIW caused suppression of both nutrient and  $\text{CO}_2$  upwelling during periods of Bering Strait  
441 closure, both in the Bering Sea and across the subarctic Pacific Ocean region.

442 Results here suggests that the regional significance of sea ice and deep water ventilation in the  
443 subarctic Pacific Ocean has been generally underestimated when modelling Quaternary climate  
444 change, where GNPIW growth and propagation from the Bering Sea influences both local and,  
445 importantly, regional upwelling of NPDW and export production. The strong correlation  
446 between high latitude upwelling and glacial cycles in atmospheric  $\text{CO}_2$  (Fig. 4b-c), and the  
447 bipolar nature of Quaternary glaciations, also supports suggestions that sea ice was a primary  
448 control on the past global climate state (Sigman et al., 2010). Overall, improved understanding  
449 of this mechanistic relationship between the Bering Sea and the subarctic Pacific will aid future  
450 efforts to constrain the role of glacial-interglacial oceanographic variability in global climate,  
451 in complement to Southern Ocean-driven dynamics.

452

## 453 **References**

454 Aguilar-Islas, A.M., Rember, R.D., Mordy, C.W., Wu, J., 2008. Sea ice-derived dissolved  
455 iron and its potential influence on the spring algal bloom in the Bering Sea. *Geophys.*

456 Res. Lett. 35, 10–14. doi:10.1029/2008GL035736

457 Asahi, H., Kender, S., Ikehara, M., Sakamoto, T., Takahashi, K., Ravelo, a. C.C., Alvarez  
458 Zarikian, C. a. A., Khim, B.K.K., Leng, M.J.J., 2016. Orbital-scale benthic foraminiferal  
459 oxygen isotope stratigraphy at the northern Bering Sea Slope Site U1343 (IODP  
460 Expedition 323) and its Pleistocene paleoceanographic significance. *Deep. Res. Part II*  
461 *Top. Stud. Oceanogr.* 125–126, 66–83. doi:10.1016/j.dsr2.2014.01.004

462 Brunelle, B.G., Sigman, D.M., Cook, M.S., Keigwin, L.D., Haug, G.H., Plessen, B.,  
463 Schettler, G., Jaccard, S.L., 2007. Evidence from diatom-bound nitrogen isotopes for  
464 subarctic Pacific stratification during the last ice age and a link to North Pacific  
465 denitrification changes. *Paleoceanography* 22, 1–17. doi:10.1029/2005PA001205

466 Cook, M.S., Ravelo, A.C., Mix, A., Nesbitt, I.M., Miller, N. V., 2016. Tracing subarctic  
467 Pacific water masses with benthic foraminiferal stable isotopes during the LGM and late  
468 Pleistocene. *Deep. Res. Part II Top. Stud. Oceanogr.* 125–126, 84–95.  
469 doi:10.1016/j.dsr2.2016.02.006

470 Detlef, H., Belt, S.T., Sosdian, S.M., Smik, L., Lear, C.H., Hall, I.R., Cabedo-Sanz, P.,  
471 Husum, K., Kender, S., 2018. Sea ice dynamics across the Mid-Pleistocene transition in  
472 the Bering Sea. *Nat. Commun.* 9. doi:10.1038/s41467-018-02845-5

473 Elderfield, H., Ferretti, P., Greaves, M., Crowhurst, S.J., McCave, I.N., Hodell, D. a,  
474 Piotrowski, A.M., 2012. Evolution of ocean temperature. *Science* (80-. ). 337, 704–709.  
475 doi:10.1594/PANGAEA.786205

476 Galbraith, E.D., Jaccard, S.L., Pedersen, T.F., Sigman, D.M., Haug, G.H., Cook, M.,  
477 Southon, J.R., Francois, R., 2007. Carbon dioxide release from the North Pacific abyss  
478 during the last deglaciation. *Nature* 449, 890–893. doi:10.1038/nature06227

479 Galbraith, E.D., Kienast, M., Jaccard, S.L., Pedersen, T.F., Brunelle, B.D., Sigman, D.M.,  
480 Kiefer, T., 2008. Consistent relationship between global climate and surface nitrate

481 utilization in the western subarctic Pacific throughout the last 500 ka. *Paleoceanography*  
482 23, 1–11. doi:10.1029/2007PA001518

483 Gong, X., Lembke-Jene, L., Lohmann, G., Knorr, G., Tiedemann, R., Zou, J.J., Shi, X.F.,  
484 2019. Enhanced North Pacific deep-ocean stratification by stronger intermediate water  
485 formation during Heinrich Stadial 1. *Nat. Commun.* 10. doi:10.1038/s41467-019-08606-  
486 2

487 Gottschalk, J., Skinner, L.C., Lippold, J., Vogel, H., Frank, N., Jaccard, S.L., Waelbroeck, C.,  
488 2016. Biological and physical controls in the Southern Ocean on past millennial-scale  
489 atmospheric CO<sub>2</sub> changes. *Nat. Commun.* 7. doi:10.1038/ncomms11539

490 Gray, W.R., Rae, J.W.B., Wills, R.C.J., Shevenell, A.E., Taylor, B., Burke, A., Foster, G.L.,  
491 Lear, C.H., 2018. Deglacial upwelling, productivity and CO<sub>2</sub> outgassing in the North  
492 Pacific Ocean. *Nat. Geosci.* 11, 340–344. doi:10.1038/s41561-018-0108-6

493 Horikawa, K., Asahara, Y., Yamamoto, K., Okazaki, Y., 2010. Intermediate water formation  
494 in the Bering Sea during glacial periods: Evidence from neodymium isotope ratios.  
495 *Geology* 38, 435–438. doi:10.1130/G30225.1

496 Jaccard, S.L., Galbraith, E.D., Sigman, D.M., Haug, G.H., 2010. A pervasive link between  
497 Antarctic ice core and subarctic Pacific sediment records over the past 800 kyrs. *Quat.*  
498 *Sci. Rev.* 29, 206–212. doi:10.1016/j.quascirev.2009.10.007

499 Jaccard, S.L., Haug, G.H., Sigman, D.M., Pedersen, T.F., Thierstein, H.R., Röhl, U., 2005.  
500 Glacial/ Interglacial Changes in Subarctic North Pacific Stratification. *Science* (80-. ).  
501 308, 1003–1006. doi:10.1126/science.1108696

502 Jaccard, S.L., Hayes, C.T., Martinez-Garcia, A., Hodell, D.A., Anderson, R.F., Sigman,  
503 D.M., Haug, G.H., 2013. Two modes of change in Southern Ocean productivity over the  
504 past million years 339, 1419–1423.

505 Jang, K., Huh, Y., Han, Y., 2017. Authigenic Nd isotope record of North Pacific Intermediate

506 Water formation and boundary exchange on the Bering Slope. *Quat. Sci. Rev.* 156, 150–  
507 163. doi:10.1016/j.quascirev.2016.11.032

508 Jouzel, J., Masson-Delmotte, V., Cattani, O., Dreyfus, G., Falourd, S., Hoffmann, G.,  
509 Minster, B., Nouet, J., Barnola, J.M., Chappel-laz, J., Fischer, H., Gallet, J.C., Johnsen,  
510 S., Leuenberger, M., Lulergue, L., Luethi, D., Oerter, H., Parrenin, F., Raisbeck, G.,  
511 Raynaud, D., Schilt, A., Schwander, J., Selmo, E., Souchez, R., Spahni, R., Stauffer, B.,  
512 Steffensen, J.P., Stenni, D., Stocker, T.F., Tison, J.L., Werner, M., Wolff, E.W., 2007.  
513 Orbital and millennial Antarctic climate variability over the last 800 000 years. *Science*  
514 (80-. ). 5839, 793–796.

515 Kender, S., Ravelo, A.C., Worne, S., Swann, G.E.A., Leng, M.J., Asahi, H., Becker, J.,  
516 Detlef, H., Aiello, I.W., Andreasen, D., Hall, I.R., 2018. Closure of the Bering Strait  
517 caused Mid-Pleistocene Transition cooling. *Nat. Commun.* 9. doi:10.1038/s41467-018-  
518 07828-0

519 Kim, S., Khim, B.K., Ikehara, M., Takahashi, K., 2017. Relationship between  $\delta^{15}\text{N}$  values of  
520 bulk sediments and total organic carbon concentration in response to orbital-scale  
521 biogenic opal production in the Bering slope area over the last 600 kyrs. *Quat. Int.* 459,  
522 144–152. doi:10.1016/j.quaint.2017.05.041

523 Kim, S., Takahashi, K., Khim, B.K., Kanematsu, Y., Asahi, H., Ravelo, A.C., 2014. Biogenic  
524 opal production changes during the Mid-Pleistocene Transition in the Bering Sea (IODP  
525 Expedition 323 Site U1343). *Quat. Res. (United States)* 81, 151–157.  
526 doi:10.1016/j.yqres.2013.10.001

527 Knudson, K.P., Ravelo, A.C., 2015a. North Pacific Intermediate Water circulation enhanced  
528 by the closure of the Bering Strait. *Paleoceanography* 30, 1287–1304.  
529 doi:10.1002/2015PA002840

530 Knudson, K.P., Ravelo, A.C., 2015b. Enhanced subarctic Pacific stratification and nutrient

531 utilization during glacials over the last 1.2 Myr. *Geophys. Res. Lett.* 42, 9870–9879.  
532 doi:10.1002/2015GL066317

533 Lam, P.J., Robinson, L.F., Blusztajn, J., Li, C., Cook, M.S., McManus, J.F., Keigwin, L.D.,  
534 2013. Transient stratification as the cause of the North Pacific productivity spike during  
535 deglaciation. *Nat. Geosci.* 6, 622–626. doi:10.1038/ngeo1873

536 Li, D., Zheng, L.W., Jaccard, S.L., Fang, T.H., Paytan, A., Zheng, X., Chang, Y.P., Kao, S.J.,  
537 2017. Millennial-scale ocean dynamics controlled export productivity in the subtropical  
538 North Pacific. *Geology* 45, 651–654. doi:10.1130/G38981.1

539 Lisiecki, L.E., Raymo, M.E., 2005. A Pliocene-Pleistocene stack of 57 globally distributed  
540 benthic  $\delta^{18}\text{O}$  records. *Paleoceanography* 20, 1–17. doi:10.1029/2004PA001071

541 Lüthi, D., Le Floch, M., Bereiter, B., Blunier, T., Barnola, J.M., Siegenthaler, U., Raynaud,  
542 D., Jouzel, J., Fischer, H., Kawamura, K., Stocker, T.F., 2008. High-resolution carbon  
543 dioxide concentration record 650,000–800,000 years before present. *Nature* 453, 379–  
544 382. doi:10.1038/nature06949

545 Matsumoto, K., Oba, T., Lynch-Stieglitz, J., Yamamoto, H., 2002. Interior hydrography and  
546 circulation of the glacial Pacific Ocean. *Quat. Sci. Rev.* 21, 1693–1704.  
547 doi:10.1016/S0277-3791(01)00142-1

548 Max, L., Lembke-Jene, L., Riethdorf, J.R., Tiedemann, R., Nürnberg, D., Kühn, H.,  
549 MacKensen, A., 2014. Pulses of enhanced north Pacific intermediate water ventilation  
550 from the Okhotsk Sea and Bering Sea during the last deglaciation. *Clim. Past* 10, 591–  
551 605. doi:10.5194/cp-10-591-2014

552 McClymont, E.L., Sostian, S.M., Rosell-Melé, A., Rosenthal, Y., 2013. Pleistocene sea-  
553 surface temperature evolution: Early cooling, delayed glacial intensification, and  
554 implications for the mid-Pleistocene climate transition. *Earth-Science Rev.* 123, 173–  
555 193. doi:10.1016/j.earscirev.2013.04.006

556 Melles, M., Minyuk, P.S., Nowaczyk, N.R., Deconto, R.M., Anderson, P.M., Andreev, A.A.,  
557 Coletti, A., Cook, T.L., Lozhkin, A. V, Tarasov, P., Vogel, H., Wagner, B., 2012. 2.8  
558 Million Years of Arctic Climate e from Lake El'gygytgyn, NE Russia. *Science* (80-. ).  
559 337, 1–8.

560 Mix, A.C., Pisias, N.G., Rugh, W., Wilson, J., Morey, A., Hagelberg, T.K., 1995. Benthic  
561 Foraminifer Stable Isotope Record from Site 849 (0-5 Ma): Local and Global Climate  
562 Changes. *Proc. Ocean Drill. Program*, 138 Sci. Results 138.  
563 doi:10.2973/odp.proc.sr.138.120.1995

564 Mizobata, K., Saitoh, S.I., 2004. Variability of Bering Sea eddies and primary productivity  
565 along the shelf edge during 1998-2000 using satellite multisensor remote sensing. *J.*  
566 *Mar. Syst.* 50, 101–111. doi:10.1016/j.jmarsys.2003.09.014

567 Ohkushi, K., Itaki, T., Nemoto, N., 2003. Last Glacial-Holocene change in intermediate-  
568 water ventilation in the Northwestern Pacific. *Quat. Sci. Rev.* 22, 1477–1484.  
569 doi:10.1016/S0277-3791(03)00082-9

570 Praetorius, S.K., Mix, A.C., Walczak, M.H., Wolhowe, M.D., Addison, J.A., Prahl, F.G.,  
571 2015. North Pacific deglacial hypoxic events linked to abrupt ocean warming. *Nature*  
572 527, 362–366. doi:10.1038/nature15753

573 Rae, J.W.B., Sarnthein, M., Foster, G.L., Ridgeway, A., Grootes, P.M., Elliott, T., 2014.  
574 Deep water formation in the North Pacific and deglacial CO<sub>2</sub> rise. *Paleoceanography* 29,  
575 1–23. doi:10.1002/2013PA002570.Received

576 Robinson, R.S., Kienast, M., Luiza Albuquerque, A., Altabet, M., Contreras, S., De Pol Holz,  
577 R., Dubois, N., Francois, R., Galbraith, E., Hsu, T.C., Ivanochko, T., Jaccard, S., Kao,  
578 S.J., Kiefer, T., Kienast, S., Lehmann, M., Martinez, P., McCarthy, M., Möbius, J.,  
579 Pedersen, T., Quan, T.M., Ryabenko, E., Schmittner, A., Schneider, R., Schneider-Mor,  
580 A., Shigemitsu, M., Sinclair, D., Somes, C., Studer, A., Thunell, R., Yang, J.Y., 2012. A



581 review of nitrogen isotopic alteration in marine sediments. *Paleoceanography* 27.  
582 doi:10.1029/2012PA002321

583 Sambrotto, R.N., Mordy, C., Zeeman, S.I., Stabeno, P.J., Macklin, S.A., 2008. Physical  
584 forcing and nutrient conditions associated with patterns of Chl a and phytoplankton  
585 productivity in the southeastern Bering Sea during summer. *Deep. Res. Part II Top.*  
586 *Stud. Oceanogr.* 55, 1745–1760. doi:10.1016/j.dsr2.2008.03.003

587 Sigman, D.M., DiFiore, P.J., Hain, M.P., Deutsch, C., Wang, Y., Karl, D.M., Knapp, A.N.,  
588 Lehmann, M.F., Pantoja, S., 2009. The dual isotopes of deep nitrate as a constraint on  
589 the cycle and budget of oceanic fixed nitrogen. *Deep. Res. Part I Oceanogr. Res. Pap.*  
590 56, 1419–1439. doi:10.1016/j.dsr.2009.04.007

591 Sigman, D.M., Hain, M.P., Haug, G.H., 2010. The polar ocean and glacial cycles in  
592 atmospheric CO<sub>2</sub> concentration. *Nature* 466, 47–55. doi:10.1038/nature09149

593 Snyder, C.W., 2016. Evolution of global temperature over the past two million years. *Nature*  
594 538, 226–228. doi:10.1038/nature19798

595 Springer, A.M., Peter McRoy, C., Flint, M. V., 1996. The Bering Sea Green Belt: Shelf-edge  
596 processes and ecosystem production. *Fish. Oceanogr.* 5, 205–223. doi:10.1111/j.1365-  
597 2419.1996.tb00118.x

598 Stabeno, P.J., Schumacher, J.D., Ohtani, K., 1999. The physical oceanography of the Bering  
599 Sea. *Dyn. Bering Sea* 1–60.

600 Stroynowski, Z., Abrantes, F., Bruno, E., 2017. The response of the Bering Sea Gateway  
601 during the Mid-Pleistocene Transition. *Palaeogeogr. Palaeoclimatol. Palaeoecol.* 485,  
602 974–985. doi:10.1016/j.palaeo.2017.08.023

603 Studer, A.S., Martínez-García, A., Jaccard, S.L., Girault, F.E., Sigman, D.M., Haug, G.H.,  
604 2012. Enhanced stratification and seasonality in the Subarctic Pacific upon Northern  
605 Hemisphere Glaciation-New evidence from diatom-bound nitrogen isotopes, alkenones

606 and archaeal tetraethers. *Earth Planet. Sci. Lett.* 351–352, 84–94.  
607 doi:10.1016/j.epsl.2012.07.029

608 Takahashi, K., Ravelo, A.C., Alvarez Zarikian, C.A., Expedition 323 Scientists, 2011. Site  
609 U1343. *Proc. IODP, 323 323*. doi:10.2204/iodp.proc.323.107.2011

610 Talley, L.D., 1993. Distribution and Formation of North Pacific Intermediate Water. *J. Phys.*  
611 *Oceanogr.* 23, 517–537.

612 Teraishi, A., Suto, I., Onodera, J., Takahashi, K., 2016. Diatom, silicoflagellate and ebridian  
613 biostratigraphy and paleoceanography in IODP 323 Hole U1343E at the Bering slope  
614 site. *Deep. Res. Part II Top. Stud. Oceanogr.* 125–126, 18–28.  
615 doi:10.1016/j.dsr2.2013.03.026

616 Tsunogai, S., Kusakabe, M., Iizumi, H., Koike, I., Hattori, A., 1979. Hydrographic features of  
617 the deep water of the Bering Sea-the sea of Silica. *Deep Sea Res. Part A, Oceanogr. Res.*  
618 *Pap.* 26, 641–659. doi:10.1016/0198-0149(79)90038-4

619 VanLaningham, S., Piasias, N.G., Duncan, R.A., Clift, P.D., 2009. Glacial-interglacial  
620 sediment transport to the Meiji Drift, northwest Pacific Ocean: Evidence for timing of  
621 Beringian outwashing. *Earth Planet. Sci. Lett.* 277, 64–72.  
622 doi:10.1016/j.epsl.2008.09.033

623 Yasuda, I., 1997. The origin of the North Pacific Intermediate Water. *J. Geophys. Res.*  
624 *Ocean.* 102, 893–909. doi:10.1029/96jc02938

## 625 **Acknowledgements**

626 We would like to thank the International Ocean Drilling Program for providing samples as well  
627 as the Expedition 323 staff and crew of the JOIDES Resolution, and the curators at the Kochi  
628 Core Centre. This research was funded by Natural Environment Research Council (NERC)  
629 Envision DTP, CASE funding from the British Geological Survey and NERC Isotope

630 Geosciences Facilities Steering Committee grant IP-1674-1116 (to S.K.). SW performed the  
631 sample preparation, statistical analyses and led the writing of the manuscript. All authors  
632 assisted in writing and contributed to interpretations on the manuscript. SK conceived the  
633 overall project and isotope analyses were overseen by MJL and CR. We are also grateful to  
634 Dyke Andreasen and Colin Carney from the Ravelo laboratory, as well as Christopher  
635 Kendrick and Jack Lacey from the NERC Isotope Geosciences Facility, for support with  
636 instrumentation and sample preparation. Further thanks is extended to Sunghan Kim and  
637 colleagues, for providing their nitrogen and carbon data from Site U1343. Finally, we would  
638 like to thank the reviewers for their helpful suggestions and comments throughout the  
639 submission process. All data needed to evaluate the conclusions in the paper are present in the  
640 paper and/or the Supplementary Materials. Additional data related to this paper may be  
641 requested from the authors.

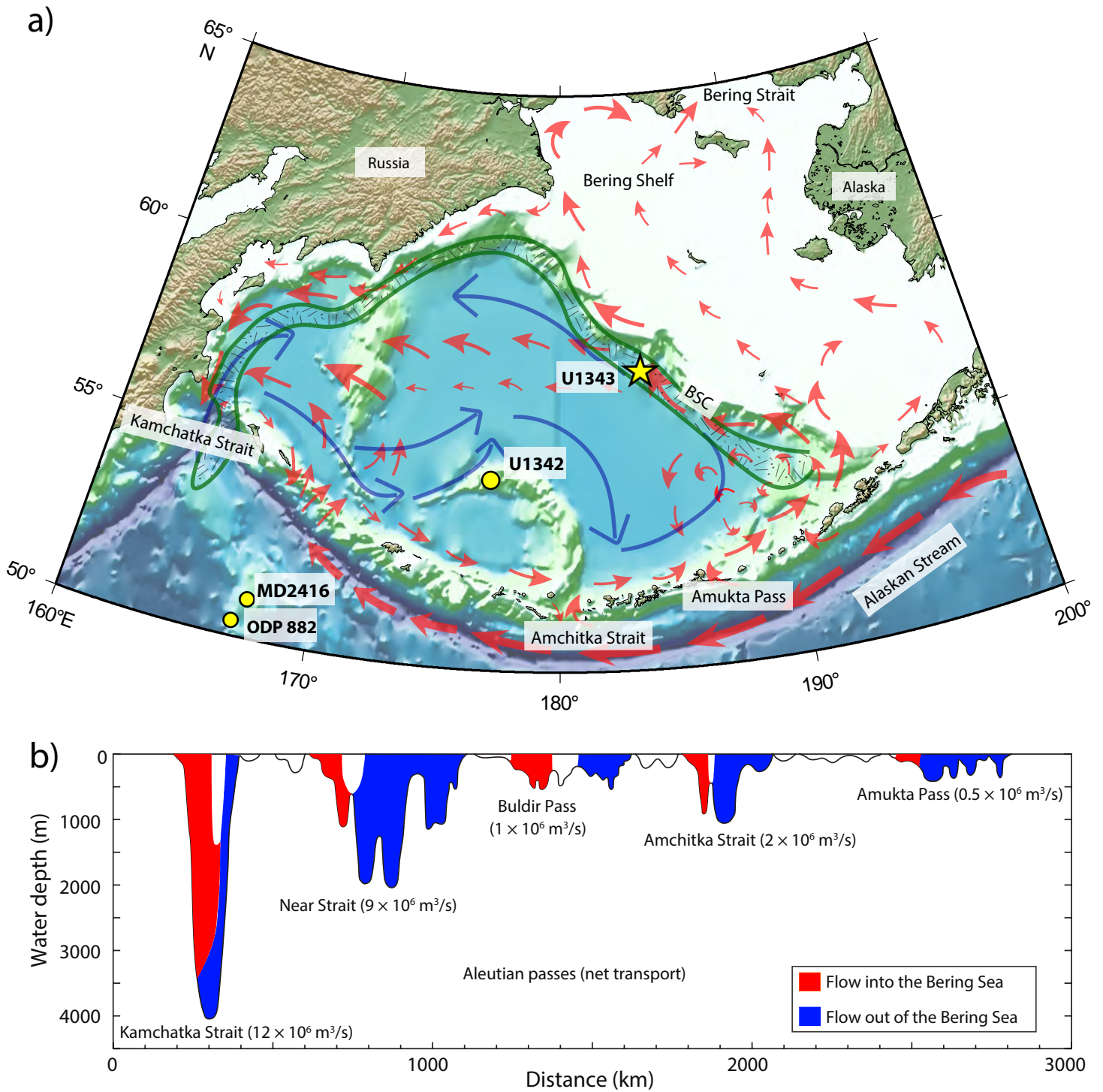


**Fig. 1: Oceanographic setting of the Bering Sea and subarctic Pacific Ocean.** **a)** Location of Site U1343 (57° 33' N, 175° 49' W; 1954 m; this study) on the Bering slope and Site U1342 (54° 83' N, 176° 92' E; 818m) in the southern Bering Sea from IODP Expedition 323. The location of North West Pacific ODP Sites 882 (50.35, 167.58; 3244 m) and MD2416 (51.27 N, 167.73 E; 2317m) are also shown, together with surface (red arrows) and deep water (blue arrows) circulation. The high productivity 'green belt' region (Springer et al., 1996), stimulated by shelf-adjacent Bering Slope Current (BSC) is also marked (green patterned band). **b)** Cross sections of the Aleutian passes and volumes of transport through which Alaskan Stream water exchanges with the Bering basin (Stabeno et al., 1999; Takahashi et al., 2011).

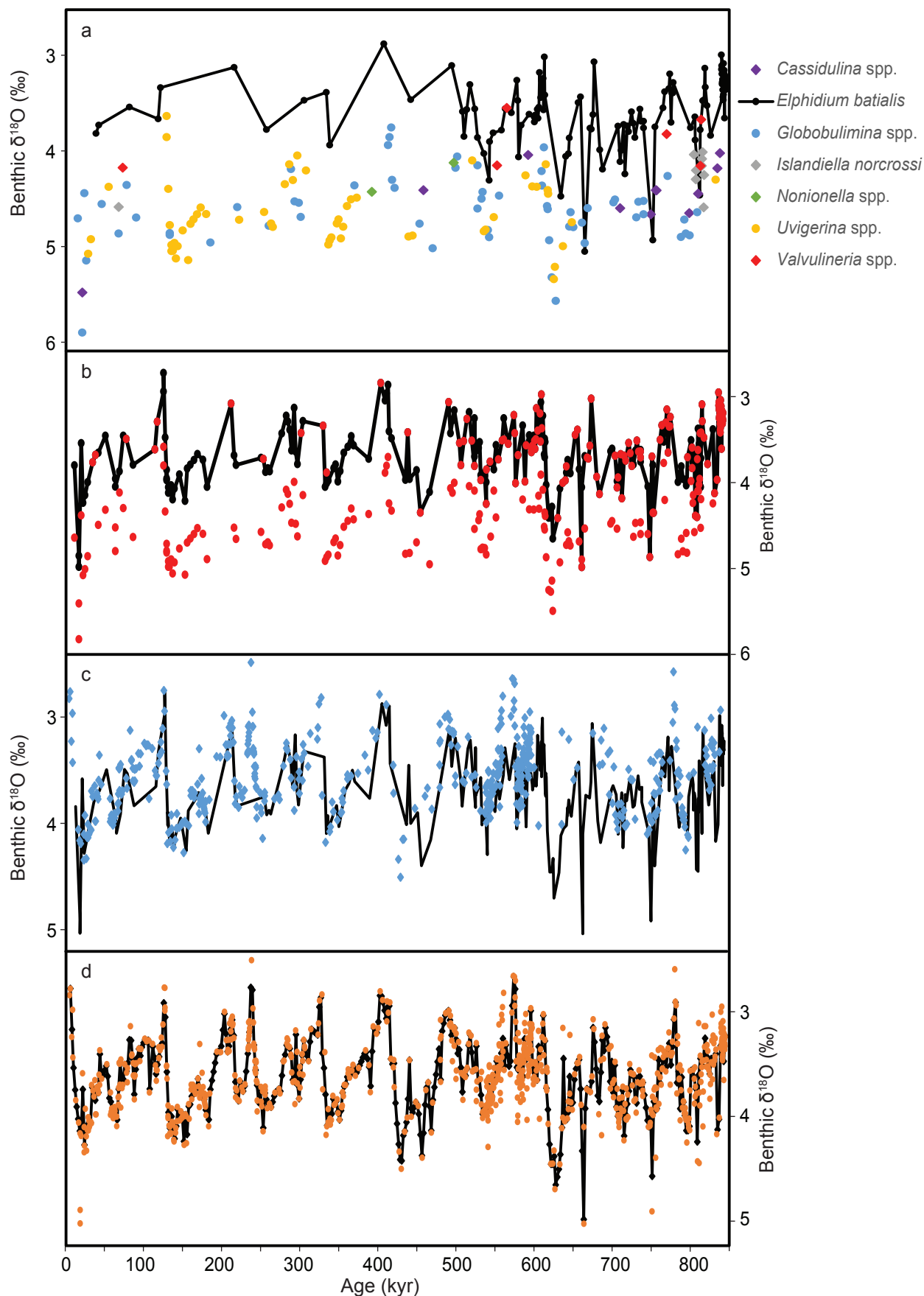


**Fig. 2 : Benthic foraminiferal  $\delta^{18}\text{O}$  results from U1343. a)** Raw  $\delta^{18}\text{O}$  values are categorised by species/genus and plotted against *E. batialis* (black) to which species-specific offsets are applied (Kender et al., 2018). **b)** Raw  $\delta^{18}\text{O}$  data (red dots) are plotted against  $\delta^{18}\text{O}_{\text{U1343}}$  (black line) which has been tuned to *E. batialis*. **c)** Comparison of  $\delta^{18}\text{O}_{\text{U1343}}$  from this study (black line) against previous data from IODP Site U1343 (Asahi et al., 2016) (blue dots), which were combined in **d)** to create the updated age model for IODP Site U1343 (orange dots), which has been smoothed using linear interpolation to a 2 kyr resolution (black line).

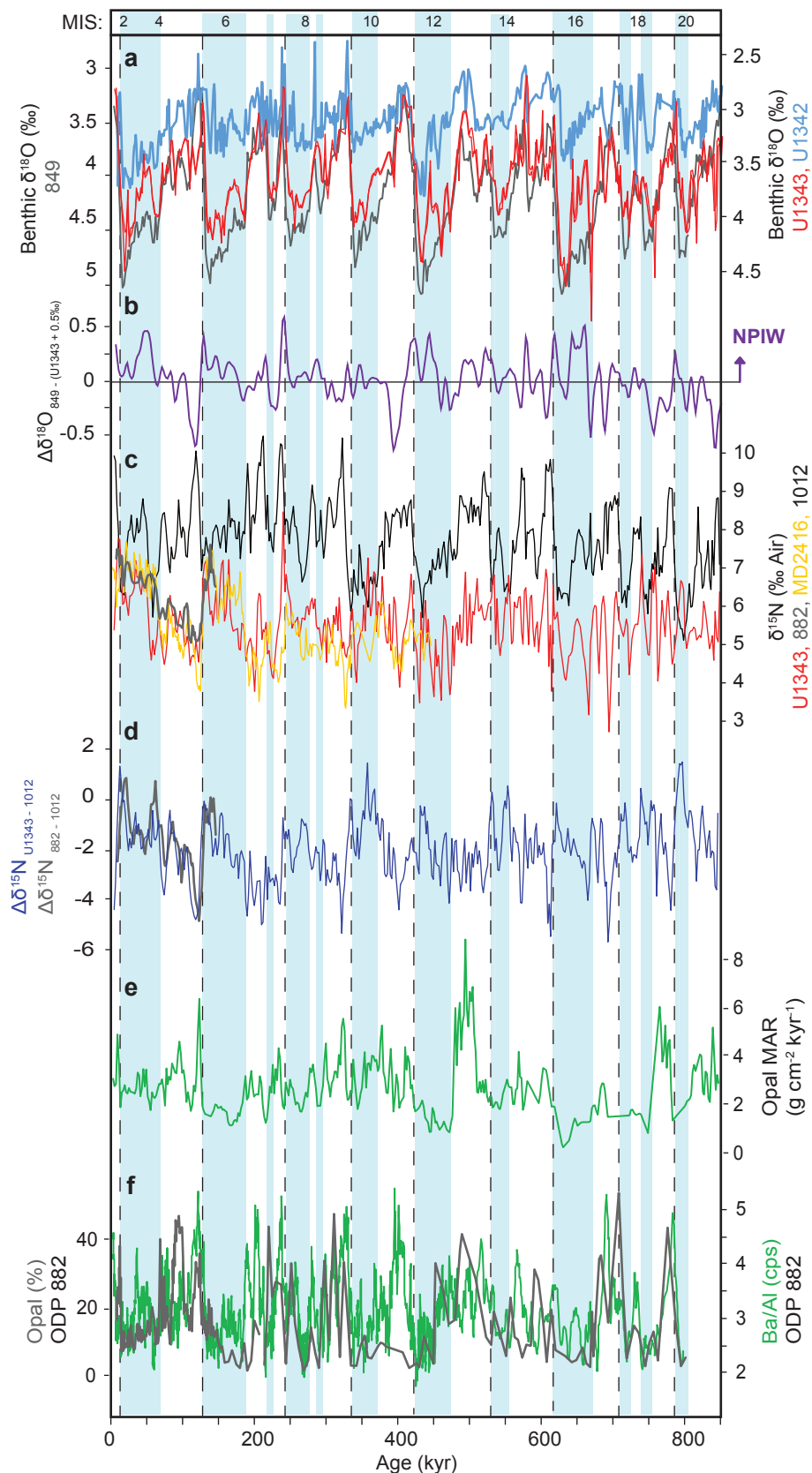


**Fig. 3: Geochemical proxy results from IODP Site U1343 from MIS 2 to 20.** **a)** Benthic foraminiferal  $\delta^{18}\text{O}$  results from IODP Site U1343 compared to those from the shallower IODP Site U1342 and deep Pacific ODP Site 849. The data from Site U1342 has been recalculated here to match benthic foraminiferal offset for *E. batialis*, used for Site U1343 (Kender et al., 2018). **b)** The offset in  $\delta^{18}\text{O}$  between IODP Site U1343 and ODP Site 849 ( $\Delta\delta^{18}\text{O}_{849-U1343}$ ). **c)** Bulk  $\delta^{15}\text{N}$  data from IODP Site U1343 compared with deep North Pacific ODP Site 1012 (a site of complete nutrient utilisation) together with bulk  $\delta^{15}\text{N}$  records from ODP Site 882 and MD2416 in the subarctic North Pacific Ocean. **d)** The  $\delta^{15}\text{N}$  offset between IODP Site U1343 and ODP Site 1012 ( $\Delta\delta^{15}\text{N}_{U1343-1012}$ ) which constrains changes in source water  $\delta^{15}\text{N}$  to reflect changes in Bering Sea nutrient utilisation. **e)** Opal mass accumulation rate (MAR) from IODP Site U1343 [adapted from Kim et al. (2014), see Methods]. **f)** The opal (%) and Ba/Al productivity records from ODP Site 882 (Jaccard et al., 2010). Blue bars represent periods of Bering Strait closure (>50 m sea level drop) (Elderfield et al., 2012) with vertical dashed lines indicating deglaciations.

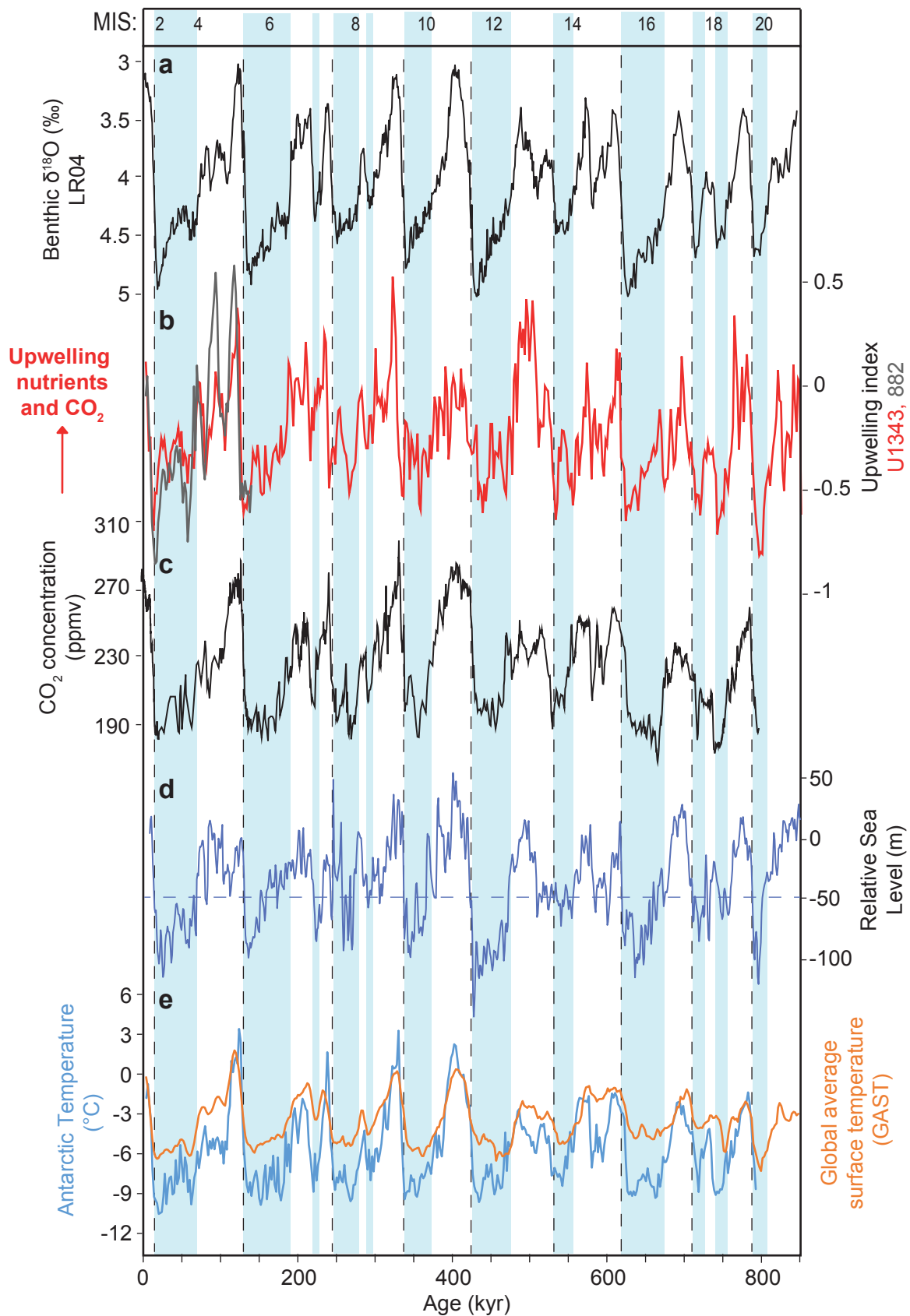
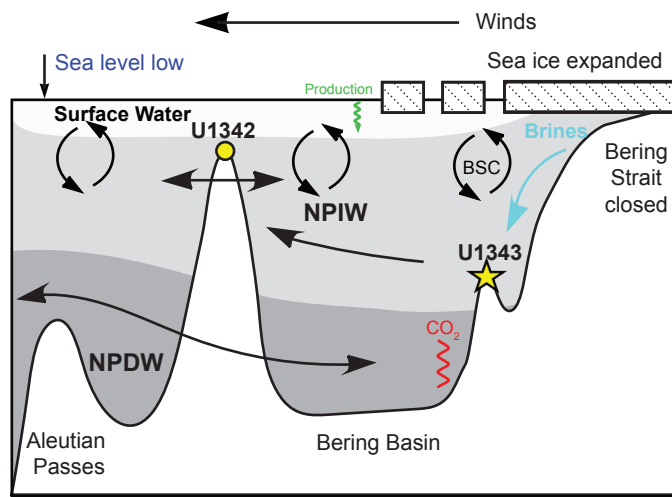
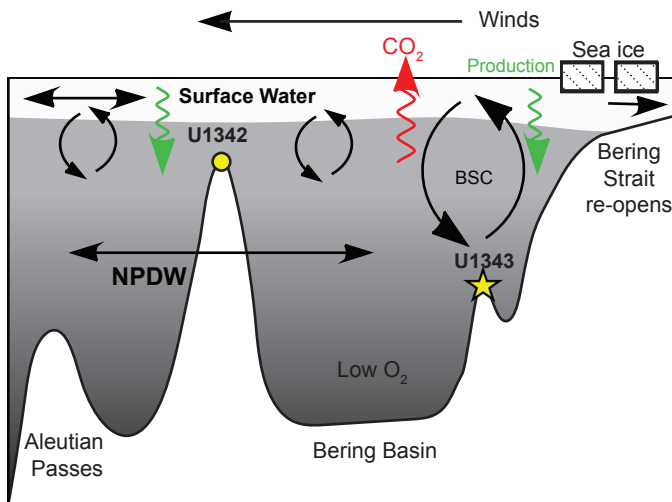


**Fig. 4: Comparison of the upwelling indexes against other global and regional paleoenvironmental records.** **a)** Composite LR04 benthic foraminiferal  $\delta^{18}\text{O}$  stack (Lisiecki and Raymo, 2005) over the last 850 kyr. **b)** The upwelling index for Site U1343 (red) and Site 882 (grey), which show suppressed rates of upwelling during glacial periods following Bering Strait closure (blue bars). The upwelling index shows strong correlation with the composite EPICA Dome C Ice Core atmospheric  $\text{CO}_2$  record over the last 800 kyr **(c)** (Lüthi et al., 2008), changes in relative sea level (m) **(d)** (Elderfield et al., 2012), where the blue lines at -50 m represent modern Bering Strait depth, and global temperature records (temperature deviation from present day) **(e)** (Jouzel et al., 2007; Snyder 2016). Vertical dashed lines indicate deglaciations.

a) Glacial: low upwelling index



b) Deglacial: high upwelling index



c) Interglacial: intermediate upwelling index

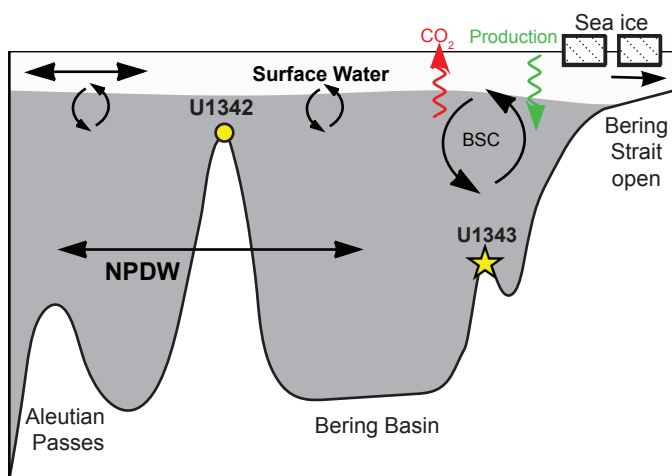


**Fig. 5: Schematic models representing glacial, deglacial and interglacial regimes of biogeochemical cycling in the Bering Sea. a)** A low upwelling index indicates reduced upwelling caused by an expansion of NPIW which forms in glacials following the closure of the Bering Strait, leading to an isolated pool of nutrients in the photic zone. This results in reduced primary productivity (opal MAR) but higher rates of nutrient utilisation due to the reduced supply of deep water nutrients into the photic zone. **b)** A high upwelling index indicates ample nutrient supply from resumed NPDW upwelling which occurs during deglaciation, leading to a high productivity/low nutrient utilisation state. **c)** An intermediate upwelling index results indicates upwelling typical of an interglacial, similar to the modern regime.



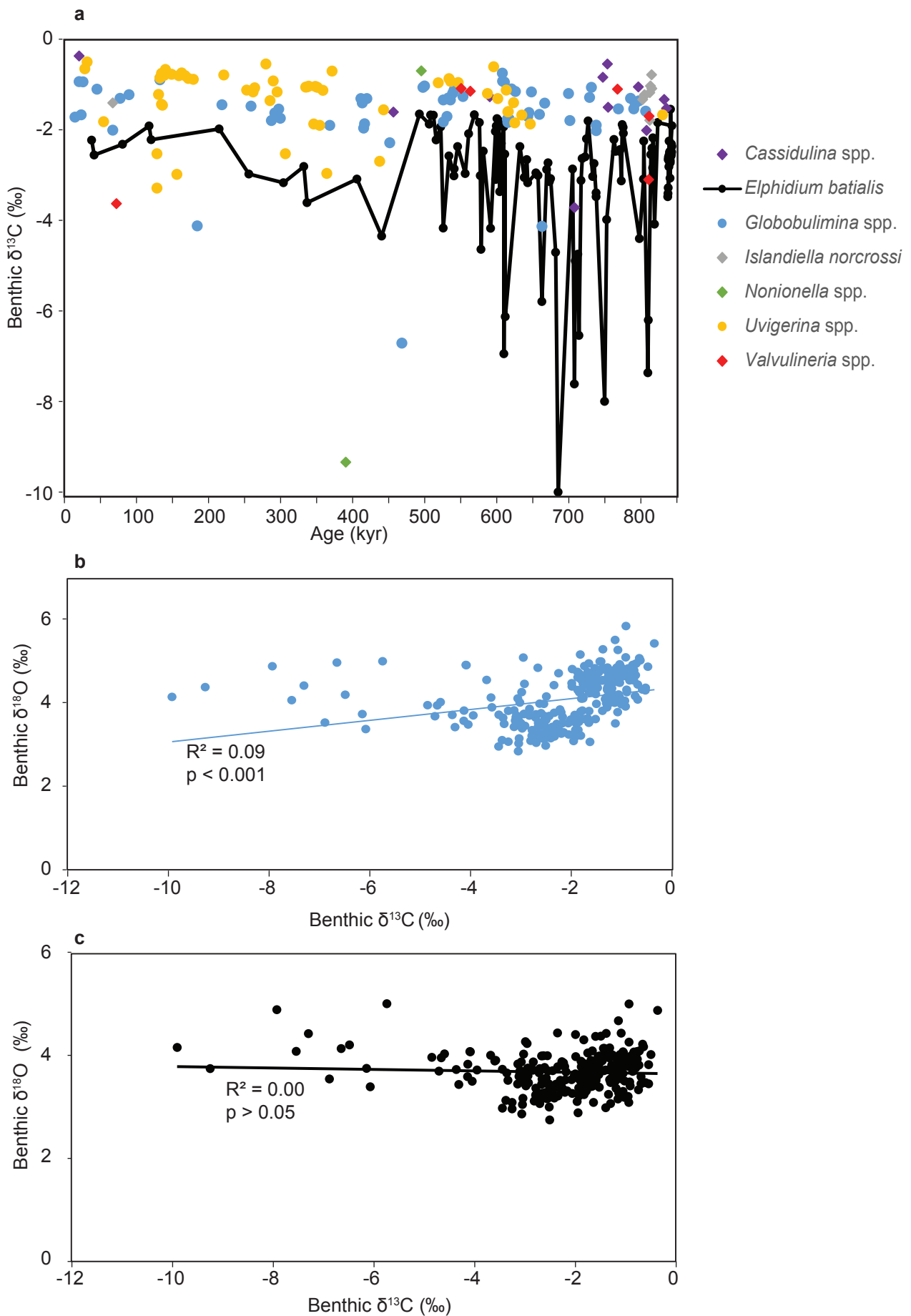


**Fig. S1: Benthic foraminiferal comparison of  $\delta^{13}\text{C}$  and  $\delta^{18}\text{O}$ .** **a)**  $\delta^{13}\text{C}$  data categorised by species/genus. The poor relationship for  $\delta^{13}\text{C}$  against both raw  $\delta^{18}\text{O}$  (**b**) and  $\delta^{18}\text{O}$  adjusted to *E. batialis* (**c**) suggests that diagenetic alteration of foraminiferal shells cannot explain the glacial-interglacial variability in the  $\delta^{18}\text{O}$ .

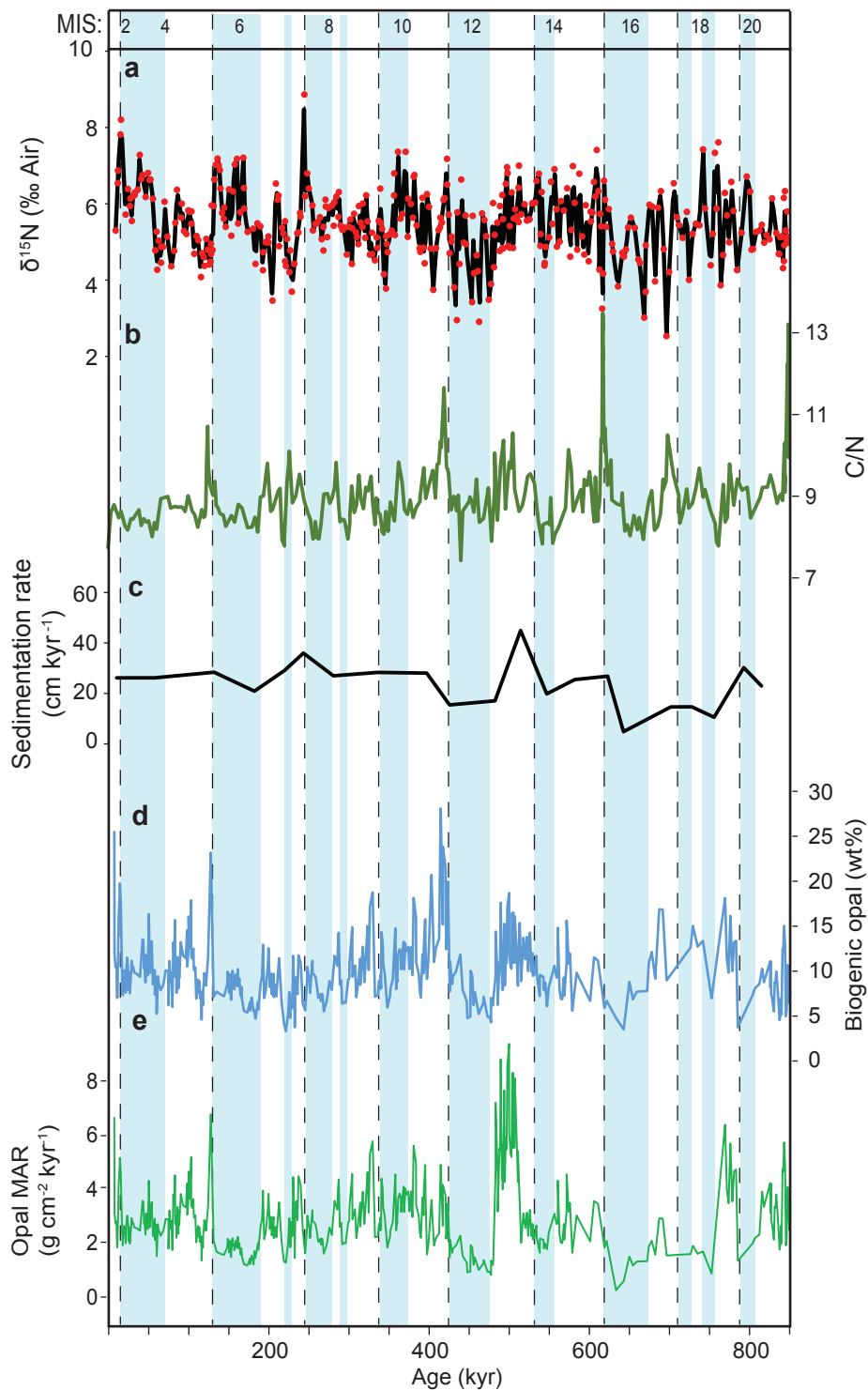


**Fig. S2: Bulk  $\delta^{15}\text{N}$  and Biogenic Opal data for IODP Site U1343.** **a)** Bulk  $\delta^{15}\text{N}$  data (red dots) from this study and previously published lower resolution data (Kim et al., 2017), smoothed using a linearly interpolation to create a 2 kyr resolution dataset (black line). **b)** C/N ratios, which are low and show a lack of covariation to  $\delta^{15}\text{N}$ , suggesting that terrestrial input of nitrogen was low and did not drive the  $\delta^{15}\text{N}$  record. **c)** New sedimentation rates calculated for IODP Site U1343 using the updated age model presented in this study, which were then applied to **d)** the biogenic opal record (Kim et al. 2014) to calculate **e)** the opal mass accumulation rate (MAR) data.

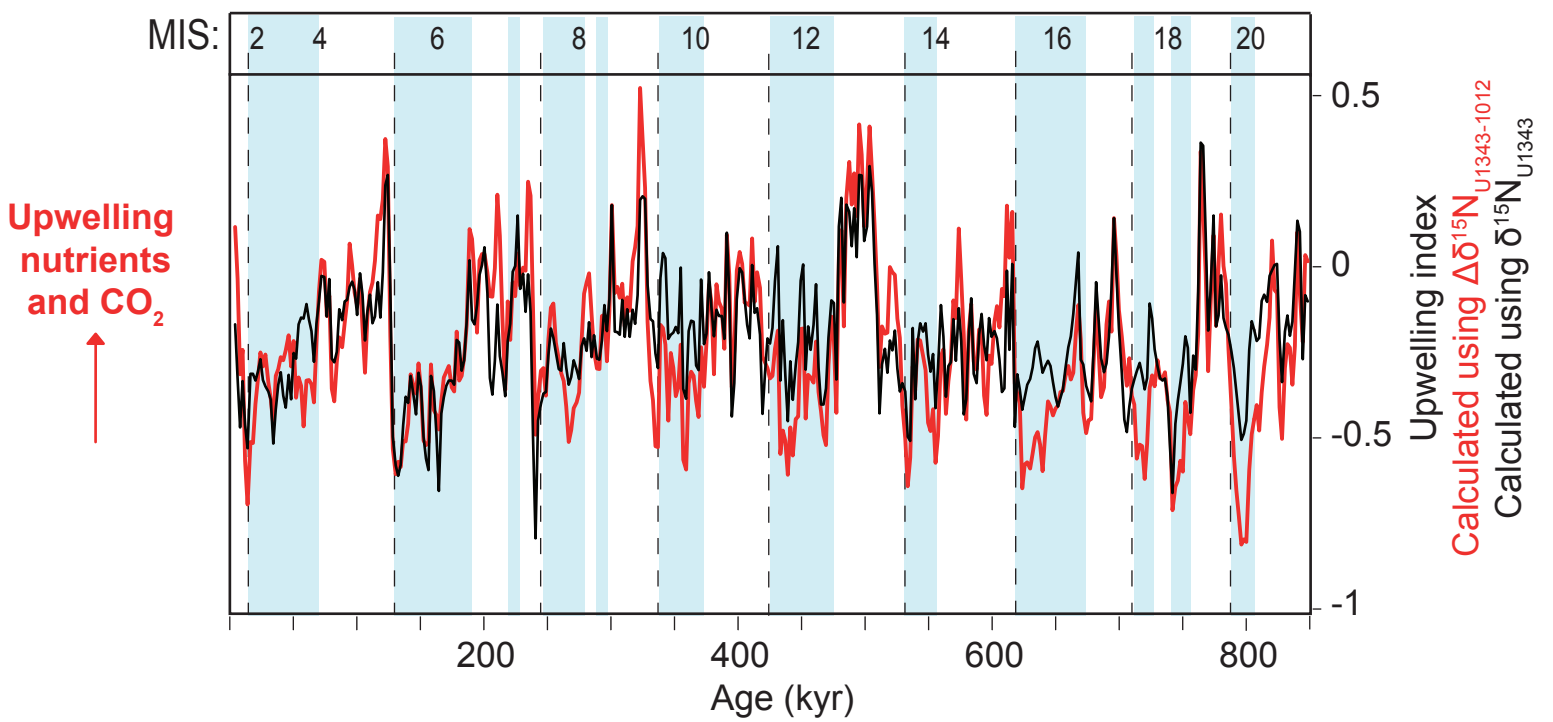


**Fig. S3: Assessing the relative contribution of  $\delta^{15}\text{N}_{1012}$  to  $\Delta\delta^{15}\text{N}_{\text{U1343-1012}}$ .** Results demonstrate that there is no significant difference between the upwelling index record calculated using  $\Delta\delta^{15}\text{N}_{\text{U1343-1012}}$  compared to  $\delta^{15}\text{N}_{\text{U1343}}$  (where the latter does not subtract the ODP 1012 record) ( $t = -1.93$ ,  $p = 0.05$ ).

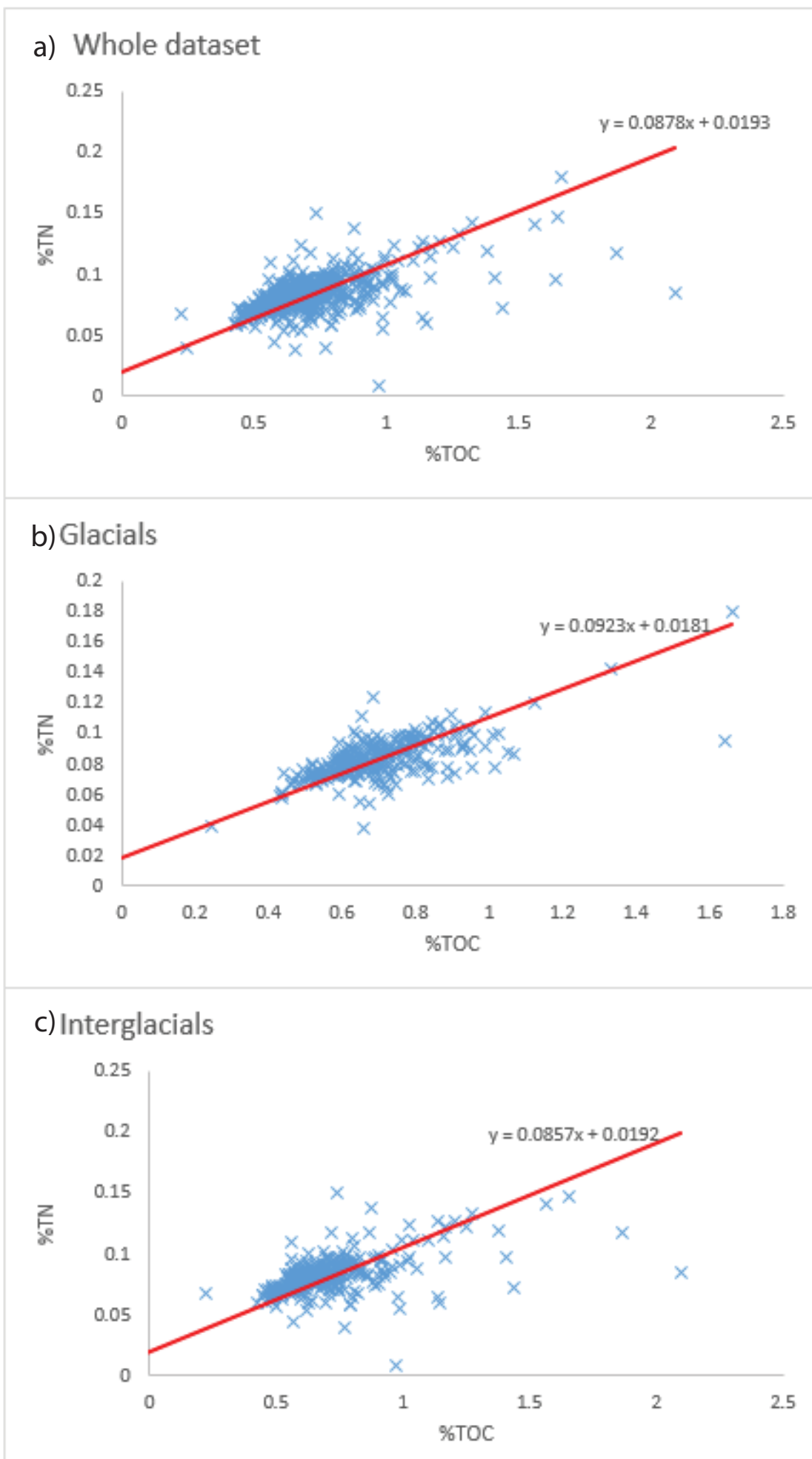


**Fig. S4: %TOC vs %TN cross plots for IODP Site U1343 from this study and previously published lower resolution data (Kim et al., 2017). a)** Shows the cross plot for the whole dataset, with an intercept of 0.0193, suggesting minimal influence of inorganic nitrogen. Similarity between **b)** glacial intercept of 0.0181 and **c)** interglacial intercept of 0.0192, suggests that variable contribution of terrestrial/inorganic nitrogen does not drive the bulk  $\delta^{15}\text{N}$  record presented here.

**Table S1: Benthic foraminiferal  $\delta^{18}\text{O}$  offsets applied to species/genus, from *Elphidium batialis* (Kender et al., 2018). The total number of samples for each group is also noted.**

| Species                      | Offset from <i>Elphidium batialis</i> (‰) | Number of samples |
|------------------------------|---|-------------------|
| <i>Elphidium batialis</i>    | 0   | 117               |
| <i>Valvulineria</i> spp.     | + 0.25                                    | 6                 |
| <i>Islandiella norcrossi</i> | + 0.48                                    | 9                 |
| <i>Cassidulina</i> spp.      | + 0.56                                    | 11                |
| <i>Nonionella</i> spp.       | + 0.65                                    | 2                 |
| <i>Globobulimina</i> spp.    | + 0.85                                    | 61                |
| <i>Uvigerina</i> spp.        | + 0.87                                    | 56                |

**Table S2: New age-depth tie points for Site U1343, building upon work of Asahi et al. (2016). Age model constructed by tuning to LR04 global benthic stack (Lisiecki and Raymo, 2005) (see Methods).**

| Depth (CCSF – A) (m) | Age (kyr) |
|----------------------|-----------|
| 0.96                 | 10.15     |
| 14.23                | 57.38     |
| 36.72                | 131.41    |
| 48.03                | 181.46    |
| 59.73                | 219.06    |
| 68.72                | 242.57    |
| 79.52                | 279.96    |
| 96.24                | 335.14    |
| 114.56               | 396.17    |
| 119.35               | 424.39    |
| 129.90               | 480.93    |
| 145.02               | 512.78    |
| 152.01               | 545.32    |
| 161.63               | 580.48    |
| 173.39               | 621.39    |
| 174.57               | 641.03    |
| 184.09               | 700.03    |
| 188.27               | 725.84    |
| 191.58               | 753.63    |
| 203.57               | 790.75    |
| 209.04               | 812.86    |